

# Cell fluorescence photoactivation as a method to select and study cellular subpopulations grown in mechanically heterogeneous environments

Julien Aureille, Mylène Pezet, Lydia Pernet, Jacques Mazzega, Alexei Grichine, Christophe Guilluy,\* and Monika Elzbieta Dolega\*

Institute for Advanced Biosciences, University Grenoble Alpes, Inserm U1209, CNRS UMR 5309 Grenoble, France

**ABSTRACT** A central challenge to the biology of development and disease is deciphering how individual cells process and respond to numerous biochemical and mechanical signals originating from the environment. Recent advances in genomic studies enabled the acquisition of information about population heterogeneity; however, these so far are poorly linked with the spatial heterogeneity of biochemical and mechanical cues. Whereas *in vitro* models offer superior control over spatiotemporal distribution of numerous mechanical parameters, researchers are limited by the lack of methods to select subpopulations of cells in order to understand how environmental heterogeneity directs the functional collective response. To circumvent these limitations, we present a method based on the use of photo convertible proteins, which when expressed within cells and activated with light, gives a stable fluorescence fingerprint enabling subsequent sorting and lysis for genomics analysis. Using this technique, we study the spatial distribution of genetic alterations on well-characterized local mechanical stimulation within the epithelial monolayer. Our method is an *in vitro* alternative to laser microdissection, which so far has found a broad application in *ex vivo* studies.

## Monitoring Editor

Diane Lidke  
University of New Mexico

Received: Nov 2, 2020

Revised: May 5, 2021

Accepted: Jun 9, 2021

## INTRODUCTION

With advances in sequencing techniques, it became clear that almost all cellular systems represent a certain degree of heterogeneity (Altschuler and Wu, 2010) resulting from intrinsic genetic programs (Chen *et al.*, 2020) or simply due to variations in complex and often dynamically changing cellular environments. The environmental factors acting on cells can be simplified into biochemical (growth factors, basement membrane composition, morphogens, etc.) and mechanical (i.e., tension, shear stress, rigidity of the environment) (Mammoto and Ingber, 2010; Janmey and Miller, 2011). Whereas for numerous simple developmental systems a full genetic picture is

available (Gilmour *et al.*, 2017), so far a limited number of techniques (Nelson, 2017; Barriga *et al.*, 2018) exist to quantify mechanical parameters arising from physiological tissue function *in vivo* or to perturb mechanically living systems and correlate spatiotemporally the mechanotransduction processes occurring in response. To overcome these limitations, numerous methods have been developed that are applicable for *in vitro* single or multicellular models (Roca-Cusachs *et al.*, 2017), improving our understanding of the role of forces on cell response (Mammoto and Ingber, 2010). Interestingly, even in those simplified experimental systems, phenotypic heterogeneity has been widely observed. For example, culturing epithelial monolayers on micropatterns gives rise to the appearance of supra-waves (Serra-Picamal *et al.*, 2012; Petrolli *et al.*, 2019) and an altered spatial distribution of proliferating cells due to the imposed border conditions and resulting local changes in monolayer tissue tension. Similarly, the use of three-dimensional (3D) multicellular spheroids under isotropic compression enables at once creating heterogeneity in oxygen and nutrient distribution (as observed in growing tumors), and at the same time correlating these with coexisting gradients of mechanical parameters (Stylianopoulos *et al.*, 2012; Dolega *et al.*, 2017). Despite the advantages in controlling numerous environmental conditions, researchers are often limited in *in vitro* studies by the lack of robust methods to select subpopulations of cells for

This article was published online ahead of print in MBoC in Press (<http://www.molbiolcell.org/cgi/doi/10.1091/mbc.E20-10-0676>) on June 16, 2021.

\*Address correspondence to: Christophe Guilluy ([Christophe.Guilluy@inserm.fr](mailto:Christophe.Guilluy@inserm.fr)); Monika Elzbieta Dolega ([Monika.Dolega@univ-grenoble-alpes.fr](mailto:Monika.Dolega@univ-grenoble-alpes.fr)).

Abbreviations used: AF, autofluorescence; AFM, atomic force microscopy; AP-TES, 3-amino-propyltriethoxysilane; FD, field diaphragm; FP, fluorescent protein; FWHM, full width at half maximum; LCM, laser capture microdissection; PA, photoactivated; PBS, phosphate-buffered saline; ROI, regions of interest.

© 2021 Aureille *et al.* This article is distributed by The American Society for Cell Biology under license from the author(s). Two months after publication it is available to the public under an Attribution–Noncommercial–Share Alike 3.0 Unported Creative Commons License (<http://creativecommons.org/licenses/by-nc-sa/3.0>).

“ASCB®,” “The American Society for Cell Biology®,” and “Molecular Biology of the Cell®” are registered trademarks of The American Society for Cell Biology.

further transcriptomic and proteomic studies in order to enable obtaining the link between mechanical, biochemical and arising genetic heterogeneities. Uncovering this correlation of heterogeneities of cells is crucial to improve our understanding of cellular communication in both healthy and pathological states.

Among the available methods allowing obtaining samples of a spatially chosen subpopulation of cells (including manual disruption, micropipette aspiration), the most commonly used and commercialized is laser capture microdissection (LCM) (Emmert-Buck *et al.*, 1996), which was developed specifically for thin (up ~20  $\mu\text{m}$  thick) fixed sections of extracted tissues and biopsies. In between various operating modes of LCM (reviewed in Datta *et al.*, 2015), the principle relies on precutting the zone of interest of the tissue sample with the laser. Despite several improvements made to extend the application of LCM over the *in vitro* models, the necessity of using specific LCM-compatible substrates for cell culture has so far limited its use in biophysical studies. Moreover, alternative methods are usually experimentally laborious. To circumvent these limitations, we propose a method applicable to a majority of *in vitro* models based on the expression of photoactivatable proteins (Patterson and Lippincott-Schwartz, 2002; Grimm *et al.*, 2016) within the cells, which when activated with light provide a fluorescent fingerprint that can be spatiotemporally controlled. After enzymatic cell dissociation, selected cells (fluorescent ones) can be isolated using commonly available flow cytometry cell sorters and processed for genomic and transcriptomic studies. This approach enables selection of subpopulation of cells not only according to their biochemical signature (presence or absence of given signaling proteins) but also according to experimentally determined mechanical conditions. We show the application of this method using a microfluidic system providing local deformation of the epithelium, which triggers the appearance of gradients of tension within the epithelial monolayer. Therefore, our method allows correlating phenotypic, morphological, and genetic changes occurring in response to mechanical stimulation.

## RESULTS AND DISCUSSION

### Photoactivation as a mean for cellular selection

Photoactivatable fluorescent proteins (PA-FPs) are characterized by their ability to switch to a new fluorescent state in response to irradiation with light of specific wavelength and intensity. The first PA-FPs were based on the irreversible photoconversion from the non-fluorescent *off* state into an activated and stable *on* state (Patterson and Lippincott-Schwartz, 2002). Further development of PA-FPs included versions that were amenable to either activation to undergo wavelength shift or reversible photoactivation. The introduction of PA-FPs has brought numerous applications, including 1) live cell tracking, 2) studies on protein diffusion and binding kinetics, 3) protein–protein interactions with modified FRET imaging, and 4) super-resolution microscopy (reviewed in Lippincott-Schwartz and Patterson, 2009). Here we introduce a new concept in which irreversible PA-FPs enable spatial selection of subpopulations of cells through flow cytometry cell sorting and further genetic analyses (comparison with LCM, Supplemental Material Annex S1). Moreover, our experiment on selective photoactivation of cells within acini (3D cellular spheres) embedded in hydrogels (Supplemental Material Annex S2) suggests a potential for this method to be used for other 3D systems such as spheroids and organoids. We use a PA-mCherry construct, which when introduced into cells (either through transfection or as a stable expression) converts from the dark state into a red fluorescence on activation with the intense violet light (390–415 nm) (Subach *et al.*, 2009) (Figure 1A).

Advances in microscopy technology allowed photoconversion of subcellular structures using targeted regions of interest (ROIs) executed with galvanometric mirrors or acousto-optic deflectors (reviewed in Ronzitti *et al.*, 2017). However, these advanced microscopes are not necessarily broadly available to all researchers willing to use our methodological concept. Therefore, to enable a wide-ranging application of PA-FPs for spatial cellular selection and sorting among biological laboratories, we decided to experimentally provide guidelines for the spatial resolution of a photoactivation spot using a basic inverted fluorescence microscope equipped with a metal-halide fluorescent light source and a typical set of objectives. The size of the photoactivation spot depends on numerous parameters such as 1) magnification (type of the objective); 2) excitation field heterogeneity, light diffraction, and reflection artifacts; 3) excitation profile; and 4) heterogeneities of photoactivatable protein concentration within cells that depend on transfection efficiency. Here we used the inverted AxioObserver microscope (Carl Zeiss) with two air objectives, the Plan-Neofluar 20 $\times$ /0.45 and the LD Plan-Neofluar 40 $\times$ /0.6, both equipped with a correction collar for glass thickness variation (0–1.5 mm). By sequentially illuminating the epithelial monolayer for 5 min with 30-ms pulses every 5 s, we defined a typical diameter of the spot to be  $669 \pm 4 \mu\text{m}$  and  $1449 \pm 23 \mu\text{m}$  for objective 40 $\times$  and 20 $\times$ , respectively (Figure 1B). Whereas it is clear that objective magnification will have the biggest influence on the photoactivation process (Figure 1C), we observed that changing the light intensity (10, 25, 50, and 100%; exact power values are presented in Supplemental Material Annex S5) resulted in the ~10% variation of the effective photoactivated (PA) spot diameter (from 750 to 671  $\mu\text{m}$ ) (Figure 1D). Since the effective PA spot size depends on the excitation light profile, we characterized this parameter as a function of excitation light intensity (Figure 1E). We observed that the spot diameter determined at FWHM (full width at half maximum) did not vary significantly with excitation intensity. However, the diffracted light halo and the light scattered by cells and their substrate spread the decreasing (from ~30% of maximum down to zero) excitation intensity up to 50  $\mu\text{m}$  (calculated for 20 $\times$  objective) distance beyond the FWHM circle. This spread light is more important with thick substrates (data not shown) and should be minimized by adjusting the correction collar of the objective. Moreover, the effective photoactivation profile was strongly affected by cell population heterogeneity (Figure 1F). To maintain a sharp excitation light profile, it is thus preferable to excite with high light intensities and for a shorter time. In parallel, excitation light intensity needs to be optimized considering photo toxicity.

To provide a mean to control the diameter of the PA spot without changing the magnification or the excitation power density, we took advantage of the presence of the epifluorescence field diaphragm (FD) that is at present standard in the majority of epifluorescence microscopes equipped with Köhler illumination. By varying the diaphragm, we were able to alter the field of illumination without changing the excitation power density by much. However, the full field excitation profile is critical in this case and should be adjusted to be as flat as possible using the lamp alignment. We measured that with the FD open to only 25%, the PA spot was significantly reduced down to  $316 \pm 41 \mu\text{m}$  and  $661 \pm 26 \mu\text{m}$  for 40 $\times$  and 20 $\times$  objective, respectively (Figure 1, B and C). When the FD was reduced further to its minimum (~10%), we achieved the spatial activation selection of  $187 \pm 21 \mu\text{m}$  in diameter with 40 $\times$  objective (that contains only few tens of cells). The obtained results on the size of the spot fall within the typical dimensions of many structural aspects of tissues (i.e., size of the villi in the intestine [Altmann and Leblond, 1970; Creff *et al.*, 2019]), developmental processes (i.e., epithelial

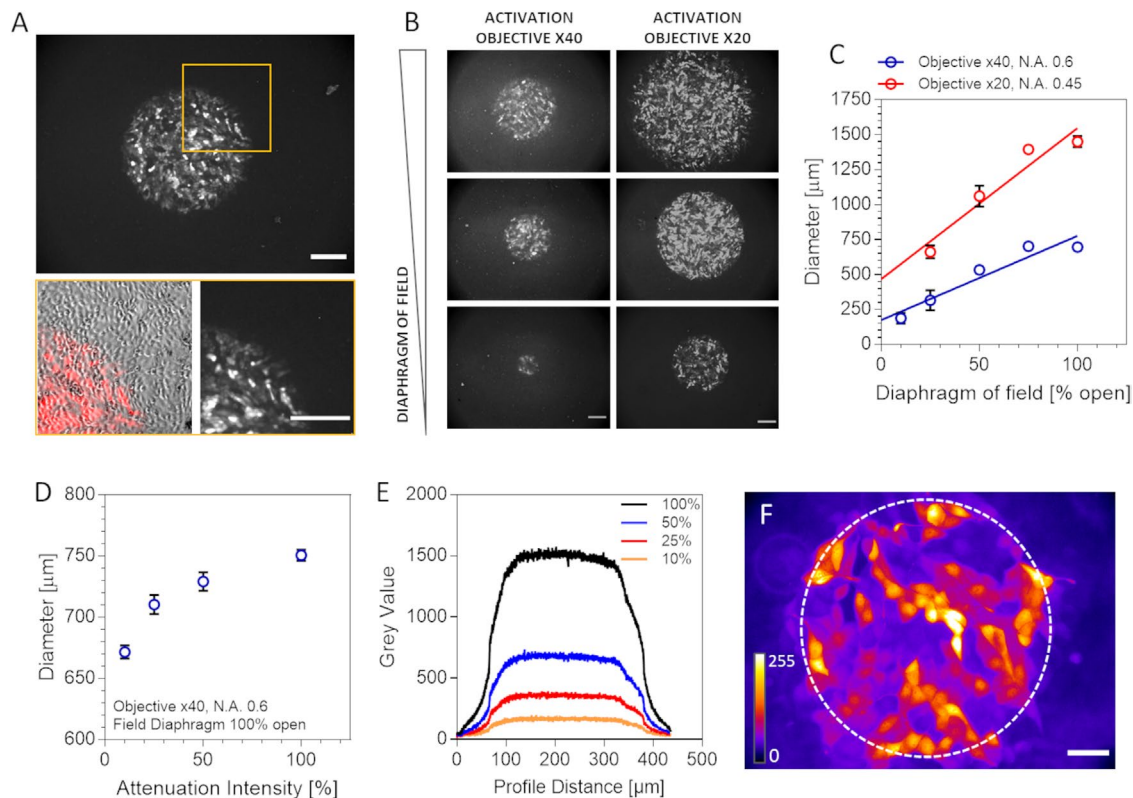


**FIGURE 1:** Effect of the FD manipulation and illumination source intensity on photoactivation spot size. (A) Images of the PA area when FD is 100% open. Orange region of interest (ROI) represents a zoom showing the bright field image merged with mCherry signal (left) and the PA mCherry cell fluorescence alone within the spot (right). Scale bar, 200  $\mu\text{m}$ . (B) Series of images showing the resulting photoactivation spot depending on the objective used for the photoactivation and reflected light (RL) diaphragm opening. Images on top correspond to 100% FD opening. Scale bar, 200  $\mu\text{m}$ . (C) Quantification of the PA spot diameter for 20 $\times$  and 40 $\times$  objective. Graph represents mean  $\pm$  SD. Each point represents three independent photoactivation spots. (D) Quantification of the effect of the lamp optical power on the photoactivation spot diameter using 40 $\times$  objective. Photoactivation was obtained by 100-ms pulses every 1 s during 5 min. Graph represents mean  $\pm$  SD. Each point represents three independent photoactivation spots. (E) Excitation light profile in the function of excitation light intensity (10–100%) for 20 $\times$  objective. (F) Fluorescent signal of mCherry within the PA spot. The false color representation of the intensity within the PA spot. The circle represents the boundary of the excitation spot (objective 20 $\times$ ). Scale bar 50  $\mu\text{m}$ .

folding [Lecuit and Lenne, 2007; Gilmour *et al.*, 2017]), and in vitro mechanical stress (Nelson *et al.*, 2005; Petrolli *et al.*, 2019).

The second important step in the application of PA-FPs for controlled spatial cellular selection for transcriptomic analyses is the monolayer enzymatic dissociation followed by flow cytometry sorting. With the highly evolving field of single cells transcriptomics and FACS on-chip (Wyatt Shields IV *et al.*, 2015), the small volume and number of cells are eventually not limiting factors. It is especially valid for in vitro experiments when numerous experimental conditions can be provided in parallel, that is, micropatterns or mechanically stimulated cells as we will present in the second part of the paper.

### Tension regulates local response within folding epithelial monolayers

Improvements in mechanical parameters analysis and techniques to induce controlled heterogeneity within the population of cells now enable directly studying the link between the mechanical state and a consequent biochemical response. To further study this link and to show the application of our PA-FP-based cell selection, we developed a microfluidic system that recreates typical gradients observed in vivo during epithelial folding by inducing a local epithelial

monolayer deformation (Figure 2A). By increasing the air pressure within the channel, cells seeded on the thin elastic PDMS membrane are stretched above the microfluidic channel. Local deformation is associated with the gradient of compression spreading laterally from the channel border (Figure 2B). Since cell size within the epithelium has been previously correlated with rigidity (Nehls *et al.*, 2019), we followed spatially the cellular Young's modulus by atomic force microscopy (AFM) before and after induced deformation. We measured changes in cell rigidity within quiescent MDCK cells monolayers ( $n_{\text{total}} = 26$  cells for  $P = 0$ ; 18 cells for  $P > 0$ ,  $t = 1$ ; 24 cells for  $P > 0$ ,  $t = 15$  min from  $N = 2$  independent experiments) and observed a significant deformation-related difference occurring for compressed cells at the close channel proximity (Figure 2C).

To further understand how the induced deformation alters cell morphology, we followed spatially the changes of nuclear height of mechanically stretched cells above the channel and compressed cells next to the channel. By fixing the samples and immunostaining for Lamin A/C, we measured nuclear height changes ( $n_{\text{total}} =$  stretched 58 cells; compressed 78 cells presented together from  $N = 2$  independent experiments) with the flattening occurring above the channel and changes occurring in cells that were in-plane compressed. These changes are well correlated spatially with the

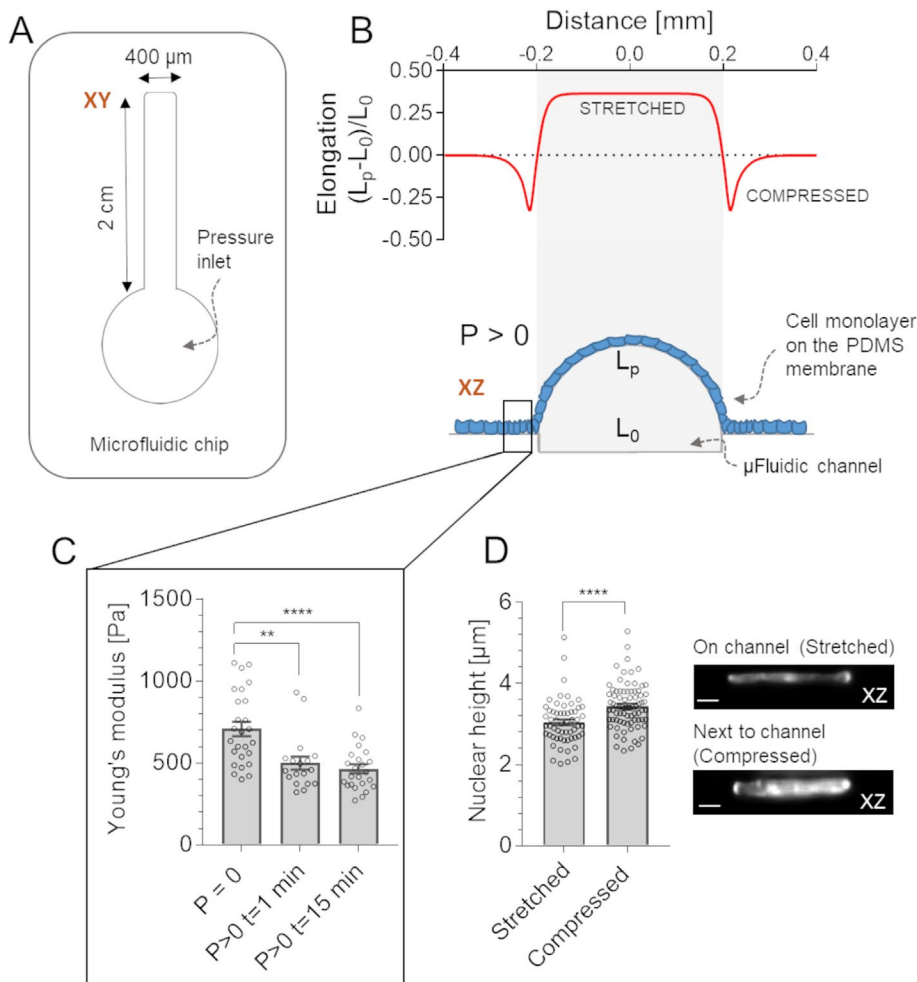


**FIGURE 2:** Spatial epithelial response to the imposed deformation. (A) Schematic representation of the microfluidic chip composed of a single channel (XY view) closed with the elastic PDMS membrane that covers also the entire surface of the chip on top of which cells form quiescent monolayers (XZ view). (B) Calculated distribution of the membrane elongation ( $L_0$  length of the channel width,  $L_p$  length of the deformed membrane) showing the regions being stretched (above the channel) and compressed (within the first 100  $\mu\text{m}$  from the channel border). (C) Changes in cellular rigidity of cells under in-plane compression. (D, on the left) Quantification of the changes in nuclear height above (stretched) and next to the channel (compressed), calculated from the Lamin A/C and Hoechst staining. Graph represents mean  $\pm$  SD from two independent experiments; unpaired Student's  $t$  test was used for statistical analysis. (On the right) Representative images of nuclear height with Lamin A/C staining. XZ view with Z-maximal projection; scale bar, 2  $\mu\text{m}$ .

strain gradient (Figure 2D). Nuclear flattening, and thus changes in nuclear shape, occurring naturally due to cellular contractility (Elosegui-Artola *et al.*, 2017) or induced experimentally (Aureille *et al.*, 2019) have shown to control gene expression. We therefore used our PA-FP-based spatial cell selection (Figure 3A) to perform transcriptomic analyses according to induced spatial cellular heterogeneities. We used MDCK stably expressing PA-mCherry and optical settings allowing photoactivation of cells along the line of 400  $\mu\text{m}$  in width corresponding to the width of the channel (Figure 3B). We selected three regions: 1) control that is positioned  $> 800 \mu\text{m}$  from the channel, 2) the zone above the channel where cells are in-plane stretched, and 3) the zone next to the channel where cells undergo in-plane compression. The mechanical deformation was applied during 4 h, the time known to induce early mechanical response (Benham-Pyle *et al.*, 2015). We photoactivated cells using short

(10 ms) and repeated (40 series) 405-nm light pulses. We verified that these parameters of photoactivation did not increase DNA damage in our epithelial monolayers (Figure 3C). The channel length of 2 cm allowed selecting  $\sim 20,000$  cells for each condition and the photoactivation process was finished within 15 min for a single experiment. Following cell selection, we used enzymatic cell dissociation using trypsin-EDTA (15 min) and obtained a single cell solution in trypsin inhibitor (to minimize the total volume and loss due to centrifugation) that we used for flow cytometry cell sorting. To minimize the effects of photoactivation on cell physiology and transcription, after photoactivation we immediately proceeded with sorting and lysis. Furthermore, sorting with the flow cytometer was performed at 4°C, the temperature at which mammalian cell transcription is inhibited (Sonna *et al.*, 2002).

Flow cytometry is a robust and high-throughput method allowing analysis of thousands of cells per second and is suitable for identifying the subpopulation of cells representing 0.1% (see a review on cell sorting; Cossarizza *et al.*, 2017). We estimated that our PA cell population ( $\sim 20,000$  cells) represents  $\sim 1.2\%$  of all the cells seeded within the microfluidic system. The throughput and final sorting yield depend on numerous parameters, including 1) hierarchical gating with doublet exclusion, 2) flow rate, 3) sample concentration, and 4) chosen precision mode for sorting, which determines the purity. In our experiment we performed initial fluorescence gating by analysis of PA-mCherry nonactivated cells (negative control) to account for autofluorescence (AF) level and set accurately a positive threshold (Figure 3D). As expected from the images of PA areas, the PA cells showed a wide heterogeneity in their global fluorescence level. However, even for the dimmest cells the intensity was largely above the AF background and so could be easily gated (PA+ gate). We sorted between

1500 and 4000 cells ( $\sim 0.5$  to 2% of the singlets cells analyzed) per condition into a minimal volume of 100  $\mu\text{l}$  of phosphate-buffered saline (PBS) within only 20 min. For less-concentrated samples and/or low volume samples, increasingly popular microfluidic cell sorters are available (Wyatt Shields IV *et al.*, 2015; Shirao *et al.*, 2018). Following the sorting, cells were lysed and concentrations between  $\sim 100 \text{ pg}/\mu\text{l}$  and 2500  $\text{pg}/\mu\text{l}$  of total RNA were obtained, and subsequently RNAseq analysis was performed.

To understand how changes in tension regulate local epithelial response, we compared the transcription levels of cells from above the channel (stretched) versus control cells and mechanically stimulated cells next to the channel (compressed) versus control cells. Our analyses identified 44 differentially expressed genes for the former condition and 116 genes for the latter (Hierarchical Clustering of Regulated Genes, Supplemental Material Annex S4). Using the

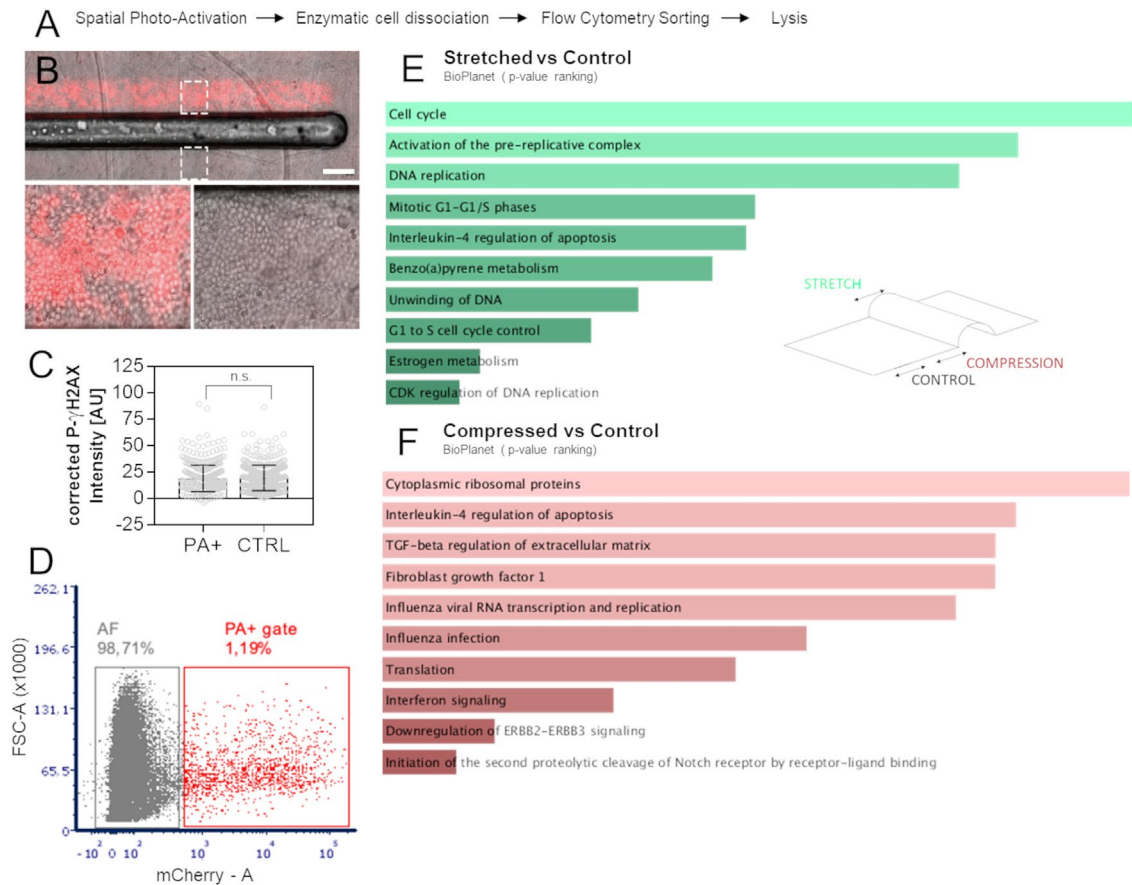


**FIGURE 3:** Locally imposed deformation defines epithelial response. (A) Brief representation of the workflow description for the photoactivation/cell sorting protocol. (B) Bright field image representing the microfluidic system with a channel and the next to the channel (compression) position of the PA region (red color, mCherry signal); Scale bar, 400  $\mu\text{m}$ . (C) Analysis of DNA damage using p- $\gamma$ H2AX immunofluorescence analysis on PA cells and the control. (D) Experimental results of the flow cytometry sorting (representing FSC forward scattering detector vs. mCherry fluorescence [610/20 nm]) showing the population of the PA cell vs. negative control cells (AF). For a detailed gating description, see Supplemental Material Annex S3. (E, F) BioPlanet database pathways analysis of the altered genes for stretched and compressed conditions, respectively. Bars represent the p value ranking. The schematic drawing shows the PA zones according to the position of the channel.

Enrichr platform (Chen *et al.*, 2013), we analyzed the BioPlanet database (Huang *et al.*, 2019) to identify globally occurring changes arising from mechanical stimulation. We observed that for stretched cells, pathways associated with cell cycle and cell cycle progression were highly affected (Figure 3E), which is in accordance to a known effect of stretch-triggering cell cycle re-entry of quiescent cells (Benham-Pyle *et al.*, 2016; Gudipaty *et al.*, 2017). Among numerous pathways for the compressed cells, we observed changes in ribosomal activity, translation, and regulation of extracellular matrix proteins (Figure 3F). The effects of compression on cell signaling are significantly less studied than those of stretched cells. Few reports are available showing that under mechanical compressive load skeletal muscle cells increase their ribosomal activity and translation (Fyfe *et al.*, 2018; Kirby, 2019), which supports our observations.

## CONCLUSIONS

Taken together, we presented a simple and broadly applicable method allowing spatial isolation of cells from *in vitro* systems. We showed an example application of our approach, which allowed selecting spatially subpopulations of cells within the epithelial monolayer and revealed that folding-like deformation within the epithelium causes spatially distributed and specific tension-related

changes in transcription. Our method approach based on photoactivatable FPs has a future potential to be used in 3D cell models (organoids and spheroids) if combined with two-photon microscopy, has a potential to be used for other *in vitro* 3D systems such as spheroids and organoids.

## MATERIALS AND METHODS

### Cell culture

MDCK II cells (Merck, #00062107-1VL) were grown in MEM (Life Technologies) supplemented with 5% fetal bovine serum (Sigma) and 1% penicillin/streptomycin (Dutscher). Cells were subcultured every 3 d when  $\sim 70\%$  confluent by using trypsin-EDTA (Dutscher). To create a dense, quiescent monolayer of MDCK, we used a calcium switch method following protocol described previously (Benham-Pyle *et al.*, 2016). For formation of the stable cell line, viruses were produced in HEK 293T cells in a 100-mm dish by simultaneous transfection of 5  $\mu\text{g}$  psPAX2 packaging vector, 2.5  $\mu\text{g}$  pVSVG envelope plasmid, and 7.5  $\mu\text{g}$  pLVX-PAmCherry-C1 vector (Ozyme #632587). The transfection media were removed and replaced after 4 h with 5 ml of complete medium. Supernatant containing lentiviral particles was harvested 48 h after transfection and filtered through a 0.45- $\mu\text{m}$  syringe filter. MDCK cells seeded in a six-well plate were transduced

with 0.5 to 1 ml of viral particles in 2.5 ml of complete medium containing polybrene 10 µg/ml (Merck). Following 48 h of culture, cells were seeded in T25 flasks and cultured for 2 wk in complete medium supplemented by puromycin 2.5 µg/ml (Merck).

### Microfabrication

The microfluidic devices were fabricated by direct milling of the channel structure in transparent, 375-µm-thick polycarbonate film (Lexan 8010, Goodfellow Cambridge) using a vertical CNC milling machine (MFG4025P, Ergwind, Poland) and a 2-flute fish-tail end-mill cutter with a diameter of 400 or 200 µm (FR208, InGraph, Poland). The engraved channels (grooves) were cleaned out with a pressure washer (K7 Premium, Karcher, Germany) to remove remaining swarfs and loosely bound bulk material formed during the milling. Further, the milled chips were washed by hand with isopropanol and deionized water and finally dried out by compressed air. Polycarbonate slabs were bonded with PDMS membrane of 20 µm thickness (Wacker, ELASTOSIL Film 2030 250/20) using 1% 3-aminopropyltriethoxysilane (APTES, Merck) as described previously (Sunkara *et al.*, 2011). Briefly, clean polycarbonate slabs were exposed to oxygen plasma for 1 min (Diener, 100% power, MHz generator) and subsequently incubated with APTES solution for 20 min. After thorough washing with dH<sub>2</sub>O and isopropanol, the polycarbonate was put in firm contact with PDMS membrane freshly activated by oxygen plasma (1 min, 100% power). The bonding occurred within the minutes that followed. Numerical analysis of the PDMS membrane deformation (elongation) caused by uniform air pressure load was performed using the finite element method and explicit solver, implemented in preprocessor Abaqus/CAE, briefly, 2D planar models of the PDMS membrane with the boundary conditions: 1) full immobilization of the membrane surface (displacements and rotation  $u_1 = u_2 = u_3 = 0$ ) in the area of membrane bonding to polycarbonate; 2) uniform air pressure load on bottom surface of the membrane in the area of the channel. Dimensions of the membrane model were identical to the experimental device. Created models were meshed with 5-µm four-noded quadrilateral elements (type CPE4). Membrane material was modeled as an elastic, isotropic material described by two parameters: Young's Modulus and Poisson's Ratio, whose values were estimated at 2.0 MPa and 0.45, respectively, based on literature data.

### Video microscopy

Live cells were visualized on the AxioObserver inverted stand (Carl Zeiss) equipped with 40× and 20× objectives, on-stage cell incubation chamber. Epifluorescence and photoactivation excitation was achieved with HXP-120 (Carl Zeiss) metal-halide fluorescence light source connected via a liquid light guide and featuring ND attenuation filters for 50, 25, and 10% of maximum. A cooled MRm3 (Carl Zeiss) camera with 2 × 2 pixel binning was used for fluorescence imaging. The manual field stop in epifluorescence channel was used to adjust the size of the photoactivation spot. Zen Blue software controlled the photoactivation frequency and image acquisition.

### AFM

For AFM measurements we added to the medium a 20-µM solution of Tris-HCl, pH 7.4 (freshly prepared) to maintain stable pH during the experiments. The system with a confluent monolayer was then carefully deposited in a Petri dish and inserted into the AFM holder (CellHesion module; JPK Instruments) mounted on an optical inverted microscope (Olympus, IX-70) and operated via JPK SPM Control Software. All experiments were carried out at 37°C using the Petri Dish Heater system. Triangular cantilevers (nano and more,

4XC-GG) with a nominal force constant of 0.04 N/m were used and calibrated using the thermal noise method. To measure cell stiffness at 50 microns from the channel, the cantilever was positioned over the cell and constant force mode (10 nN) was used for all measurements. Prior to fitting the Hertz model corrected by the tip geometry to obtain Young's Modulus (Poisson's ratio of 0.5), the offset was removed from the baseline, contact point was identified, and cantilever bending was subtracted from all force curves.

### Flow cytometry cell sorting

Systems with MDCK PA-mCherry monolayers were kept under static concave deformation during 4 h. Subsequently, the pressure was turned off and systems were transferred onto an inverted motorized TIRF microscope (iMIC 2.0, TILL Photonics-FEI) equipped with lasers, an EM-CCD iXon U897 camera (Andor), and a 40× LD Air objective (N.A. 1.0). A tile region parallel to the channel was designed to activate a line of 400-µm width of cells automatically with the TIRF 0° angle mode. The whole tile was sequentially illuminated 40× for 10 ms each round (15 min total photoactivation time). Once photoactivated, monolayers were washed three times with PBS (without Ca<sup>2+</sup> and Mg<sup>2+</sup>) and incubated with trypsin-EDTA for 15 min. We used trypsin inhibitor and passed the solution of cell suspension through a mesh filter (40 microns) to discard any large aggregates. Cells were then analyzed by flow cytometry on a jet-in-air cell sorter (AriaIII, BD-Biosciences). PA-mCherry was excited by the 561-nm laser and collected through a 600 LP filter and 610/20 emission filters. Cell suspension was run through a 100-micron nozzle at a sheath pressure of 20 psi and a drop-drive frequency of 30 MHz. The flow rate was set at 2 with a threshold rate around 500 events/s. The purity sort mode was chosen. PA-mCherry positive cells were collected in a 1.5-ml Eppendorf tube containing 100 µl of PBS. During sorting, cells were maintained at 4°C to slow down possible transcriptional changes. We determined the sorting gates using a negative control (cells non-PA) and positive control (cells collectively PA by 1-min continuous exposure to 405 nm fluorescence on the inverted epifluorescence microscope equipped with 5× air objective). Sorted fraction (PA+ mCherry) was subsequently lysed with 300 µl of lysis buffer (RNA extraction kit, ThermoFisher, AM1931) and snap-frozen in liquid nitrogen.

### Image acquisition and analysis

Cells were fixed with 3.7% paraformaldehyde (Sigma) for 20 min, permeabilized with 0.1% Triton in PBS (Sigma), then washed with PBS and blocked with a blocking solution (2.5% bovine serum albumin in PBS Tween 0.2%) for 1 h. Samples were incubated overnight at 4°C with primary antibody (lamin A/C, Abcam 26300; p-γH2AX, Millipore 05636) in blocking solution, followed by three washes with PBS Tween 0.2%. The cells were then incubated with secondary antibody at room temperature for 1 h followed by three washes with PBS Tween 0.2%. After two washes with PBS, samples were finally mounted using mounting medium with DAPI (Prolong—Invitrogen). For p-γH2AX, cells were imaged using inverted epifluorescence microscopy with a Plan-Neofluar 20×/0.5 objective; p-γH2AX fluorescent was calculated following this formula: CTNF = integrated density–(area of nucleus × mean fluorescence of background readings). For nuclear height measurement, cells were observed using a Spinning Disk Andromeda (iMIC 2.0, TILL photonics-FEI) (EMCCD iXon 897 Camera with alpha-Plan Apo 63×/1.46 oil objective) and Lamin A/C was imaged with a z-step of 200 nm. Nuclear height measurements were then performed using the reslice mode in ImageJ and fitting rectangle function. Images presented in Figure 1 were obtained using an epifluorescence microscope Zeiss AxioObserver Z1 equipped with CoolSnap CDD, CoolSnap CCD camera, CO<sub>2</sub>, and

temperature controller. We used manual control over the RL diaphragm of field that was originally provided with the microscope. For photoactivation we used objectives as indicated in the figure legend. Determination of the size of the PA spot was performed in ImageJ. Briefly, PA spots with either 20× or 40× objective were subsequently imaged with 10× objective in order to visualize the full area of the spot within the field of view. Five spots per conditions were imaged. Using the circle tool, a circle was fit and adjusted manually around the spot. For imaging we used Plan Neofluar objective 20× (air, N.A 0.5) and 40× Plan-Apochromat (water, N.A. 1.0).

### RNA sequencing and analysis

Total RNA was isolated using the RNAqueous Micro Kit (Ambion) following the protocol including DNase I treatment. After quantification and quality control using the Bioanalyzer RNA 6000 Pico kit (Agilent), total RNA amounts were adjusted and libraries were prepared using the Smart-Seq Stranded kit (Takara Bio) with 500 pg RNA input and 6 min of fragmentation. The library quality control was performed with the Bioanalyzer High Sensitivity DNA kit (Agilent). Single-end RNA sequencing was carried out from three biological replicates per condition on Illumina NextSeq 500 (76 bp read, dually indexed, 1% PhiX control, and 1.1 pM loading concentration). RNA-Seq data analysis was performed by GenoSplice technology. Sequencing, data quality, reads repartition (e.g., for potential ribosomal contamination), and insert size estimation were performed using FastQC, Picard-Tools, Samtools, and rseqc. Reads were mapped using STARv2.4.0 on the canFam3 Dog genome assembly. Gene expression regulation study was performed as already described (PMID: 26584541). Briefly, for each gene present in the Dog ensemble 98 annotations, reads aligning on transcripts were counted. Based on these read counts, normalization and differential gene expression were performed using DESeq2 on R (v.3.2.5). Only genes expressed in at least one of the two compared experimental conditions were further analyzed. Genes were considered as expressed if their rpkm value was greater than 75% of the background rpkm value based on intergenic regions. Results were considered statistically significant for uncorrected *p* values ≤ 0.05 and fold changes ≥ 1.5. Clusterings and heatmaps have been performed using “dist” and “hclust” functions in R, using Euclidean distance and Ward agglomeration method. Analysis for BioPlanet terms was performed using the Enrichr online platform.

### Statistical analysis

Statistical analysis was performed using GraphPad Software. Data are presented as mean ± SD or SEM as indicated in the figure legends. Unpaired *t* test has been used unless stated otherwise. Besides transcription factor activity analysis (as described above), no exclusion criteria were used. The numbers of independent experiments performed for all of the quantitative data are indicated in the figure legends.

### ACKNOWLEDGMENTS

The authors thank the Center for Gastrointestinal Biology and Disease and Advanced Analytics Core (National Institutes of Health P30 DK34987), especially Gabrielle Cannon at the University of North Carolina. M.E.D is supported by French National Agency of Research (Grant ANR-17-CE13-0006). C.G. is supported by grants from the European Research Council (ERC) under European Union's Horizon 2020 research and innovation program (ERC Starting Grant No. 639300).

### REFERENCES

- Altmann GG, Leblond CP (1970). Factors influencing villus size in the small intestine of adult rats as revealed by transposition of intestinal segments. *Am J Anat* 127, 15–36.
- Altschuler SJ, Wu LF (2010). Cellular heterogeneity: Do differences make a difference? *Cell* 141, 559–563.
- Aureille J, Buffière-Ribot V, Harvey BE, Boyault C, Pernet L, Andersen T, Bacola G, Balland M, Fraboulet S, Landeghem LV, Guilly C (2019). Nuclear envelope deformation controls cell cycle progression in response to mechanical force. *EMBO Rep* 20, e48084.
- Barriga EH, Franze K, Charras G, Mayor R (2018). Tissue stiffening coordinates morphogenesis by triggering collective cell migration in vivo. *Nature* 554, 523–527.
- Benham-Pyle BW, Pruitt BL, Nelson WJ (2015). Mechanical strain induces E-cadherin-dependent Yap1 and β-catenin activation to drive cell cycle entry. *Science* 348, 1024–1027.
- Benham-Pyle BW, Sim JY, Hart KC, Pruitt BL, Nelson WJ (2016). Increasing β-catenin/Wnt3A activity levels drive mechanical strain-induced cell cycle progression through mitosis. *Elife* 5, 1–28.
- Chen BJ, Wu JS, Tang YJ, Tang YL, Liang XH (2020). What makes leader cells arise: Intrinsic properties and support from neighboring cells. *J Cell Physiol* 235, 8983–8995.
- Chen EY, Tan CM, Kou Y, Duan Q, Wang Z, Meirelles GV, Clark NR, Ma'ayan A (2013). Enrichr: Interactive and collaborative HTML5 gene list enrichment analysis tool. *BMC Bioinformatics* 14.
- Cossarizza A, Chang H-D, Radbruch A, Akdis M, Andrä I, Annunziato F, Bacher P, Barnaba V, Battistini L, Bauer WM, et al. (2017). Guidelines for the use of flow cytometry and cell sorting in immunological studies. *Eur J Immunol* 47, 1584–1797.
- Creff J, Courson R, Mangeat T, Foncy J, Souleille S, Thibault C, Besson A, Malaquin L (2019). Fabrication of 3D scaffolds reproducing intestinal epithelium topography by high-resolution 3D stereolithography. *Biomaterials* 221, 119404.
- Datta S, Malhotra L, Dickerson R, Chaffee S, Sen CK, Roy S (2015). Laser capture microdissection: Big data from small samples. *Histol Histopathol* 30, 1255–1269.
- Dolega ME, Delarue M, Ingremau F, Prost J, Delon A, Cappello G (2017). Cell-like pressure sensors reveal increase of mechanical stress towards the core of multicellular spheroids under compression. *Nat Commun* 8, 1–9.
- Elosegui-Artola A, Andreu I, Beedle AEM, Lezamiz A, Uroz M, Kosmalska AJ, Oria R, Kechagia JZ, Rico-Lastres P, Roux A-LL, et al. (2017). Force triggers YAP nuclear entry by regulating transport across nuclear pores. *Cell* 171, 1397–1410.e14.
- Emmert-Buck MR, Bonner RF, Smith PD, Chuaqui RF, Zhuang Z, Goldstein SR, Weiss RA, Liotta LA (1996). Laser capture microdissection. *Science* 274, 998–1001.
- Fyfe JJ, Bishop DJ, Bartlett JD, Hanson ED, Anderson MJ, Garnham AP, Stepto NK (2018). Enhanced skeletal muscle ribosome biogenesis, yet attenuated mTORC1 and ribosome biogenesis-related signalling, following short-term concurrent versus single-mode resistance training. *Sci Rep* 8, 1–21.
- Gilmour D, Rembold M, Leptin M (2017). From morphogen to morphogenesis and back. *Nature* 541, 311–320.
- Grimm JB, English BP, Choi H, Muthusamy AK, Mehl BP, Dong P, Brown TA, Lippincott-Schwartz J, Liu Z, Lionnet T, et al. (2016). Bright photoactivatable fluorophores for single-molecule imaging. *Nat Methods* 13, 985–988.
- Gudipaty SA, Lindblom J, Loftus PD, Redd MJ, Edes K, Davey CF, Krishnegowda V, Rosenblatt J (2017). Mechanical stretch triggers rapid epithelial cell division through Piezo1. *Nature* 543, 118–121.
- Huang R, Grishagin I, Wang Y, Zhao T, Greene J, Obenaus JC, Ngan D, Nguyen DT, Guha R, Jadhav A, et al. (2019). The NCATS BioPlanet – An integrated platform for exploring the universe of cellular signaling pathways for toxicology, systems biology, and chemical genomics. *Front Pharmacol* 10, 445.
- Janmey PA, Miller RT (2011). Mechanisms of mechanical signaling in development and disease. *J Cell Sci* 124, 9–18.
- Kirby TJ (2019). Mechanosensitive pathways controlling translation regulatory processes in skeletal muscle and implications for adaptation. *J Appl Physiol* 127, 608–618.
- Lecuit T, Lenne P-F (2007). Cell surface mechanics and the control of cell shape, tissue patterns and morphogenesis. *Nat Rev Mol Cell Biol* 8, 633–644.

- Lippincott-Schwartz J, Patterson GH (2009). Photoactivatable fluorescent proteins for diffraction-limited and super-resolution imaging. *Trends Cell Biol* 19, 555–565.
- Mammoto T, Ingber DE (2010). Mechanical control of tissue and organ development. *Development* 137, 1407–1420.
- Nehls S, Nöding H, Karsch S, Ries F, Janshoff A (2019). Stiffness of MDCK II cells depends on confluency and cell size. *Biophys J* 116, 2204–2211.
- Nelson CM (2017). From static to animated: Measuring mechanical forces in tissues. *J Cell Biol* 216, 29.
- Nelson CM, Jean RP, Tan JL, Liu WF, Sniadecki NJ, Spector Aa, Chen CS (2005). Emergent patterns of growth controlled by multicellular form and mechanics. *Proc Natl Acad Sci USA* 102, 11594–11599.
- Patterson GH, Lippincott-Schwartz J (2002). A photoactivatable GFP for selective photolabeling of proteins and cells. *Science* (80-) 297, 1873–1877.
- Petrolli V, Goff ML, Tadrous M, Martens K, Allier C, Mandula O, Hervé L, Henkes S, Sknepnek R, Boudou T, et al. (2019). Confinement-induced transition between wavelike collective cell migration modes. *Phys Rev Lett* 122, 1–5.
- Roca-Cusachs P, Conte V, Trepats X (2017). Quantifying forces in cell biology. *Nat Cell Biol* 19, 742–751.
- Ronzitti E, Ventalon C, Canepari M, Forget BC, Papagiakoumou E, Emiliani V (2017). Recent advances in patterned photostimulation for optogenetics. *J Opt* 19.
- Serra-Picamal X, Conte V, Vincent R, Anon E, Tambe DT, Bazellieres E, Butler JP, Fredberg JJ, Trepats X (2012). Mechanical waves during tissue expansion. *Nat Phys* 8, 628–634.
- Shrirao AB, Fritz Z, Novik EM, Yarmush GM, Schloss RS, Zahn JD, Yarmush ML (2018). Microfluidic flow cytometry: The role of micro-fabrication methodologies, performance and functional specification. *TECHNOLOGY* 6, 1–23.
- Sonna LA, Fujita J, Gaffin SL, Lilly CM (2002). Highlighted topics molecular biology of thermoregulation invited review: Effects of heat and cold stress on mammalian gene expression. *J Appl Physiol* 92, 1725–1742.
- Stylianopoulos T, Martin JD, Chauhan VP, Jain SR, Diop-Frimpong B, Bardeesy N, Smith BL, Ferrone CR, Hornicek FJ, Boucher Y, et al. (2012). Causes, consequences, and remedies for growth-induced solid stress in murine and human tumors. *Proc Natl Acad Sci USA* 109, 15101–15108.
- Subach FV, Patterson GH, Manley S, Gillette JM, Lippincott-Schwartz J, Verkhusha VV (2009). Photoactivatable mCherry for high-resolution two-color fluorescence microscopy. *Nat Methods* 6, 153–159.
- Sunkara V, Park DK, Hwang H, Chantiwas R, Soper SA, Cho YK (2011). Simple room temperature bonding of thermoplastics and poly(dimethylsiloxane). *Lab Chip* 11, 962–965.
- Wyatt Shields C IV, Reyes CD, López GP (2015). Microfluidic cell sorting: A review of the advances in the separation of cells from debulking to rare cell isolation. *Lab Chip* 15, 1230–1249.